https://doi.org/10.1016/j.est.2020.101432

Mathematical modeling and numerical analysis of the discharge process of an alkaline zinc-cobalt battery

Yanyi Ma[1], Xu Xiao[1], Wentao Yu[1], Wenxu Shang[1], Peng Tan[1,*], Zhen Wu[2], Meng Ni[3,4,*]

1 Department of Thermal Science and Energy Engineering, University of Science and Technology of China, Hefei 230026, Anhui, China
2 Shaanxi Key Laboratory of Energy Chemical Process Intensification, School of Chemical Engineering and Technology, Xi'an Jiaotong University, Xi'an 710049, Shaanxi, China
3 Department of Building and Real Estate, The Hong Kong Polytechnic University, Hung Hom, Kowloon, Hong Kong, China
4 Environmental Energy Research Group, Research Institute for Sustainable Urban Development (RISUD), The Hong Kong Polytechnic University, Hung Hom, Kowloon, Hong Kong, China

*Corresponding Authors: pengtan@ustc.edu.cn (Peng Tan); meng.ni@polyu.edu.hk (Meng Ni)

Abstract: Zinc-cobalt batteries with cobalt oxide (Co_3O_4) as the positive electrode material are promising energy storage devices, due to their safety, remarkable energy densities, and good cycle stability. To understand the discharge characteristics of an alkaline zinc-cobalt battery for design optimization, a mathematical model of the discharge process is established based on the single-domain method, which couples the species transport in the porous electrodes with the electrochemical reactions. After model validation, the effects of different design parameters on the discharge performance of zinc-cobalt batteries are investigated, and the design strategies for the battery are proposed. It is found that a thin cathode with a large porosity can lead to a high specific capacity, and a low loading with a large electroactive area is beneficial for a high discharge voltage. The separator thickness has little effect on the discharge performance of the battery. Using the electrolyte with a high concentration is

favorable for the improvement of the output voltage. The results obtained from this work can provide useful guidance for improving the discharge performance of aqueous zinc-cobalt batteries.

Keywords: Zinc-cobalt battery; Aqueous electrolyte; Mathematical modeling; Numerical analysis; Design optimization

1. Introduction

With the rapid development of electric vehicles and the continuing decline of traditional fossil fuels, it is of great demand to explore advanced energy storage systems with high energy densities and low costs [1–5]. Li-ion batteries, owing to their high energy efficiency, long service life, and remarkable energy densities (theoretical value: ~400 Wh kg^{-1}), have been widely used in daily life and are considered as one of the most promising energy storage systems [6–9]. Nevertheless, some critical problems need to be solved for Li-ion batteries, including high prices, insufficient capacities, and safety problems [10,11]. Hence, it is in great need to explore new battery systems with high energy densities, low prices, and intrinsic safety [12,13].

Rechargeable zinc-based batteries with aqueous electrolytes have allured much attention owing to the low prices, high theoretical capacities, and intrinsically safety, which are expected to be the alternatives for Li-ion batteries [14–16]. So far, a variety of zinc-based batteries have been extensively studied, such as Zn-Mn [17–20], Zn-Ni [21–23], Zn-Ag [24–27], and Zn-air batteries [28]. The configurations and reaction mechanisms of the former three are similar and all of them are closed systems. Zn-air batteries are half-open systems that deliver a remarkable energy density owning to that oxygen is directly absorbed from the

air instead of storing in the battery. However, the existing problems of Zn-based batteries are also apparent. For example, the reversibility of Zn-Mn batteries during cycling needs to be further improved, the cycle stability of Zn-Ni batteries is insufficient, and the price of Zn-Ag batteries is quite high [24]. Due to the sluggish kinetics of oxygen reactions on the air electrode, the discharge and charge voltage gaps of Zn-air batteries are usually large [28].

In addition to addressing the above-mentioned issues of rechargeable Zn-based batteries, exploring positive electrode materials with high capacities to improve the energy densities is also necessary. Cobalt oxide (Co_3O_4), as one kind of transition metal oxides, has been applied as the positive electrode material in Zn-based batteries in recent years due to its excellent theoretical capacity in alkaline electrolytes, which is up to 446 mAh g^{-1}. Wang et al. reported an alkaline Zn-Co_3O_4 battery by using electrodeposited ultrathin porous Co_3O_4 nanosheets, which demonstrated a high energy density of 241 Wh kg^{-1}, a high discharge voltage up to 1.78 V, and remarkable cycling stability (up to 2000 cycles with a high capacity retention of 80%) [29]. Using the electrode made up of Co_3O_4 nanowire-assembled clusters, Tan and coworkers reported a Zn-Co_3O_4 battery that exhibited an energy density up to 239 Wh kg^{-1}, and the capacity retention achieved 84.1% after 1000 cycles [30]. Ma et al. reported a Co^{3+} rich-Co_3O_4 nanorod material to form a Zn-Co_3O_4 battery with greatly enhanced electrochemical kinetics. The battery could work well in a mild aqueous electrolyte, delivering a high capacity of 205 mAh g^{-1}, a high discharge voltage up to 2.2 V at 0.5 A g^{-1}, and long cycling lifespan with a high capacity retention of 92% even after 5000 cycles [31]. Although the operating voltage of a mild zinc-cobalt battery is high, the existing problems are also apparent. On the one hand, the stability of the zinc electrode in mild electrolytes is

restricted by the hydrogen evolution reaction, the dendrite growth, and the formation of electrochemically inert zinc hydrate [32,33]. On the other hand, the theoretical capacity of Co_3O_4 in mild electrolytes is much lower than that in alkaline electrolytes owing to the two-electron transfer in mild electrolytes ($Co_3O_4 \rightarrow CoO$) instead of the four-electron transfer in alkaline electrolytes ($Co_3O_4 \rightarrow CoO_2$). To this end, the alkaline Zn-Co_3O_4 battery is still focused, although some crucial problems need to be solved [31].

It should be noted that most works on zinc-cobalt batteries focus on experimental tests. Although experiments are important to determine the characteristics of the battery, the time is long and the cost is high, and many design parameters are difficult to be determined accurately. The establishment of mathematical models of the complex electrochemical and transport behaviors inside the batteries can not only gain important insights into the mechanisms but also provide a significant reference for the battery design, which is very helpful to improve the battery performance [34].

In this work, we investigated the discharge performance of an alkaline zinc-cobalt battery using mathematical modeling and numerical simulations. The main research contents are as follows: a mathematical model is firstly established for coupling the species transport with electrochemical reactions in the porous electrodes. After model validation, the influences of design parameters on the battery performance are studied, including the electrode thickness, porosity, electroactive area, and electrolyte concentration. The optimization scheme of the battery design is also proposed.

2. Model development

As schematically shown in **Fig. 1**, a zinc-cobalt battery can be regarded as a porous,

multi-component and multi-phase media: the negative electrode is formed by electrodepositing metallic zinc on the carbon fiber, the positive electrode is formed by electrodepositing ultrathin porous Co_3O_4 nanosheets on the Ni foam, both of which are porous structures [29]. The substrates (carbon fiber and Ni foam) do not contribute to electrochemical reactions and acts as current collectors. The separator is usually made of a combination of nylon, cellophane, and cellulose and saturated with the electrolyte composed of concentrated potassium hydroxide (KOH). The electrochemical reactions inside the battery can be expressed as follows:

Positive electrode:

$$CoO_2 + H_2O + e^- \longrightarrow CoOOH + OH^- \quad \text{(I)}$$

$$3CoOOH + e^- \longrightarrow Co_3O_4 + OH^- + H_2O \quad \text{(II)}$$

Negative electrode:

$$Zn + 4OH^- \longrightarrow [Zn(OH)_4]^{2-} + 2e^- \quad \text{(III)}$$

$$[Zn(OH)_4]^{2-} \longrightarrow ZnO + 2OH^- + H_2O \quad \text{(IV)}$$

Total reaction:

$$2Zn + 3CoO_2 \longrightarrow Co_3O_4 + 2ZnO \quad \text{(V)}$$

During discharge, Zn reacts with OH^- anions from the alkaline electrolyte to form $[Zn(OH)_41^{2-}$ complex, which is transformed into ZnO when the concentration reaches saturation (Reaction IV). At the same time, CoO_2 is turned into Co_3O_4 and OH^- by removing oxygen and reacting with H_2O from the electrolyte [35,36]. Since a battery system is extremely complex with a variety of species transport and electrochemical reaction processes, for simplicity, the assumptions made in this work are as follows:

(1) The mass convection in the battery is neglected, and only diffusion is considered;

(2) This model describes an isothermal process, and the temperature changes are neglected.

Thus, a one-dimensional isothermal model is developed, which includes three domains: the positive porous electrode, the negative porous electrode, and the separator. With this information, the battery performance can be evaluated and the battery design can be optimized.

2.1 Governing equations

In general, the reactions can be expressed as:

$$\sum_j v_j M_j^{z_j} = n_j e^- \tag{1}$$

in which v_j is the stoichiometric coefficient, M_j is a general chemical formula for each species, z_j is the charge number, and n_j is the number of transferred electrons.

The rate of species generation at the electrode/electrolyte interface (indicated by *se* subscript) can be determined as:

$$r_{se} = -\sum_j \left(\frac{v_j}{n_j F} i_{nj} \right) \tag{2}$$

where the rate of generation/consumption is determined by the Butler-Volmer equation as [37]:

$$i_{nj} = i_{oj} \left\{ \prod_i \left(\frac{C_i}{C_{i,ref}} \right)^{pi} \prod_k \left(\frac{M_k}{M_{k,ref}} \right)^{pk} exp\left(\frac{\alpha_{aj} n_j F \eta}{RT} \right) - \prod_i \left(\frac{C_i}{C_{i,ref}} \right)^{qi} \prod_k \left(\frac{M_k}{M_{k,ref}} \right)^{qk} exp\left(\frac{-\alpha_{cj} n_j F \eta}{RT} \right) \right\} \tag{3}$$

where i_{oj} is the exchange current density, C and C_{ref} are concentration of OH ions at the electrode/electrolyte interface and the reference state, respectively. M_k is molar density of

species *k*. *F* is the Faraday's constant, *R* is the universal gas constant, and *T* is the battery temperature. The anodic and cathodic charge transfer coefficients (α_{aj} and α_{cj}) are usually obtained from experimental tests with the following condition:

$$\alpha_{aj} + \alpha_{cj} = 1 \tag{4}$$

And the overpotential η is defined as:

$$\eta = \Phi_s - \Phi_e - U_{j,ref} \tag{5}$$

in which Φ_s and Φ_e are potentials at the solid electrode and the liquid electrolyte, respectively. $U_{j,ref}$ is the equilibrium potential of each reaction. All reactions occur at the electrode/electrolyte surface.

At the positive electrode, the total generated current is related to both Reactions I and II. Therefore, the Butler-Volmer equation should be obtained for each reaction as follows:

$$i_{n2} = i_{o2}\left\{\left(\frac{C_{OH^-}}{C_{OH^-,ref}}\right)\left(\frac{M_{\mathrm{CoOOH}}}{M_{CoO_2,ref}}\right)exp\left(\frac{\alpha_{a2}F\eta_2}{RT}\right) - \left(\frac{M_{CoO_2}}{M_{CoO_2,ref}}\right)exp\left(\frac{-\alpha_{c2}F\eta_2}{RT}\right)\right\} \tag{6a}$$

$$i_{n1} = i_{o1}\left\{\left(\frac{C_{OH^-}}{C_{OH^-,ref}}\right)\left(\frac{M_{Co_3O_4}}{M_{\mathrm{CoOOH}}}\right)exp\left(\frac{\alpha_{a1}F\eta_1}{RT}\right) - \left(\frac{M_{\mathrm{CoOOH}}}{M_{\mathrm{CoOOH},ref}}\right)^3 exp\left(\frac{-\alpha_{c1}F\eta_1}{RT}\right)\right\} \tag{6b}$$

At the negative electrode, the Butler-Volmer equation can be simplified since there is only one reaction:

$$i_{n3} = i_{o3}\left\{\left(\frac{C_{OH^-}}{C_{OH^-,ref}}\right)^4\left(\frac{M_{Zn}}{M_{Zn,ref}}\right)exp\left(\frac{2\alpha_{a3}F\eta_3}{RT}\right) - \left(\frac{C_{ZnO}}{C_{Zn,ref}}\right)exp\left(\frac{-2\alpha_{c3}F\eta_3}{RT}\right)\right\} \tag{6c}$$

In a multi-phase, multi-component system such as the porous electrodes, the electrochemical processes are dominated by the conservation of mass, conservation of chemical species, and conservation of electrical charge in each phase. Here, the above-mentioned conservation laws are detailedly discussed.

2.1.1 Conservation of mass

Since cobalt oxides have different density, the porosity of the positive electrode changes according to the electrochemical reactions. A mass balance can be used to determine the porosity change of the positive electrode:

$$\frac{\partial \varepsilon_s}{\partial t} = -\frac{1}{F}\left(\frac{3MW_{CoOOH}}{\rho_{CoOOH}} - \frac{MW_{Co_3O_4}}{\rho_{Co_3O_4}}\right) a_{Co_3O_4} i_{n,1} - \frac{1}{F}\left(\frac{MW_{CoO_2}}{\rho_{CoO_2}} - \frac{MW_{CoOOH}}{\rho_{CoOOH}}\right) a_{Co_3O_4} i_{n,2} \tag{7a}$$

where *MW* denotes the molecular weight and a is the electroactive surface of the positive electrode. The first term on the right-hand side of the above equation indicates the volumetric change of the electrode due to the conversion of CoO_2 to CoOOH (Reaction I) while the second term indicates the volumetric change due to the conversion of CoOOH to Co_3O_4 (Reaction II).

A similar equation can be obtained for porosity change of the zinc electrode:

$$\frac{\partial \varepsilon_s}{\partial t} = \frac{1}{2F}\left(\frac{MW_{Zn}}{\rho_{Zn}} - \frac{MW_{ZnO}}{\rho_{ZnO}}\right) a_{Zn} i_{n,3} \tag{7b}$$

2.1.2 Conservation of species

The micro-macroscopic model for the conservation of species is:

$$\frac{\partial\left(\varepsilon c_{OH}\right)}{\partial t} = \nabla \cdot \left(D_k^{\text{eff}} \cdot \nabla c_{OH}\right) + \sum_m \left(J^d + J^\Gamma\right) - i^{\overrightarrow{OH}} \cdot \nabla\left(\frac{t_k}{zF}\right) \tag{8}$$

The terms J^d and J^Γ represent the interfacial transfers of species in electrolyte due to the microscopic diffusion and the interface movement, respectively, and t_k is the transference number of the electrolyte. In the reaction interface, the interfacial transport of species becomes:

$$J_{km}^{d} + J_{km}^{\Gamma} = -a_{km} \sum_{j} \left(\frac{t_k}{zF} + \frac{v_j}{n_j F} \right) \bar{i}_{nj} \tag{9}$$

Simplify this equation for Zn-Co_3O_4 batteries, the conservation of species takes the form:

$$\frac{\partial \left(\varepsilon c_{OH} \right)}{\partial t} = \nabla \cdot \left(D_{\text{eff}}^{OH} \nabla c_{OH} \right) - \left(\frac{t_-^o + 1}{F} + \nabla \left(\frac{t_-^o}{zF} \right) \right) j^{OH} \tag{10}$$

The total current density can be found from the following relations:

For the positive electrode:

$$j^{OH} = a_{Co_3O_4} \left(i_{n1} + i_{n2} \right) \tag{11a}$$

For the negative electrode:

$$j^{OH} = a_{Zn} i_{n3} \tag{11b}$$

The effective diffusion coefficient appeared in Eq. 10 is related to its bulk value based on Bruggeman relation:

$$D_{eff}^{OH} = \varepsilon_e^{1.5} D^{OH} \tag{12}$$

2.1.3 Conservation of electrical charge

The averaged micro-macroscopic equation for the conservation of charge is expressed as:

For the solid phase:

$$\nabla \cdot \left(\sigma^{\text{eff}} \nabla \Phi_s \right) + \sum_{m} I_{sm} = 0 \qquad m \neq s \tag{13a}$$

For the electrolyte phase:

$$\nabla \cdot \left(\kappa^{\text{eff}} \nabla \Phi_e \right) + \nabla \cdot \left(\kappa_D^{\text{eff}} \nabla \ln c_{OH} \right) + \sum_{m} I_{em} = 0 \qquad m \neq e \tag{13b}$$

where I_{sm} and I_{em} are the interfacial current density at the interface between phase m and solid and electrolyte phases, respectively. Combining Eqs. 11a and 11b gives the following forms:

$$\nabla \cdot \left(\sigma^{\text{eff}} \nabla \Phi_s \right) - j^{OH} = 0 \tag{14a}$$

and

$$\nabla \cdot \left(k^{\text{eff}} \nabla \Phi_e \right) + \nabla \cdot \left(k_D^{\text{eff}} \ln c_{OH} \right) + j^{OH} = 0 \tag{14b}$$

Here the effective electric conductivity, σ^{eff} , are corrected using the Bruggeman relation:

$$\sigma^{\text{eff}} = \sum_k \sigma_k m^{1.5} \tag{15}$$

where *m* is the mass fraction of each species in the solid phase. In the same manner, the effective ionic conductivity (κ^{eff}), is calculated using the following equation:

$$\kappa^{\text{eff}} = \frac{\varepsilon_e F^2}{RT} \left(D_{K^+} + D_{OH^-} \right) c_{OH} \tag{16}$$

2.2 Boundary conditions

The boundary conditions at all outer boundaries for concentration and potential in the electrolyte are:

$$\frac{\partial c}{\partial n} = \frac{\partial \Phi_e}{\partial n} = 0 \tag{17}$$

The boundary condition for the potential in solid is $\frac{\partial \Phi_s}{\partial n} = 0$ except for current collectors. At the negative current collector, $\Phi_s = 0$ is chosen as the reference for voltage. At the positive current collector, $\frac{\partial \Phi_s}{\partial n} = -\frac{I}{\sigma^{\text{eff}}}$ is applied for the constant current condition ($i = -i_{app}$).

3. Numerical Results

3.1 Numerical conditions

The initial conditions are specified for the separator and electrode thicknesses, the specific surface area, the porosity, and the electrolyte concentration. The values applied in this mathematical model are summarized in **Table 1**.

A finite element method was used to discretize the above boundary conditions and conservation equations. The reaction processes and the transport equations varied with time. In the case of the relative tolerance was less than 10^{-3}, the solution was thought to be

converged. The discharge voltage was obtained according to Eq. 14 in each time step and the cut-off voltage is 1.4 V. Comparing the simulated results with experimental data, the calculation was performed based on the discharge current densities of 3, 5, 8, and 10 A g^{-1}, respectively.

3.2 Model validation

To verify the developed model, the discharge curves of a zinc-cobalt battery at different current densities are compared with the experimental results from Wang's work [29] under the same operating conditions. **Fig. 2** is the comparison of the simulation results and the experimental data, from which the trends of discharge voltages are consistent. Among them, the calculated results show good agreement with the experimental data under small current densities (3 and 5 A g^{-1}). Especially, at 3 A g^{-1}, the maximum error is only 20 mV. With an increase of the current density, the error between calculations and experiments increases, and the maximum error is 0.12 V. The reasons are analyzed as follows: the present model only considers diffusion of species but convection can be non-negligible at high current densities due to high electrochemical reaction rate. Besides, this model describes the isotherm process without considering the temperature change, but the temperature rise could be significant at high current densities. We also verified the model by comparing the experimental results from Tan's work in which the negative electrode is a Zn foil [30]. Some adjustments are made to the model and some parameters with changed values are listed in **Table S1** in Supporting Information. **Fig. S1** shows the 1D model geometry of this zinc-cobalt battery. As shown in **Fig. S2**, the modeling results show good agreement with the experiment data. To sum up, the one-dimensional isotherm model demonstrates good accuracy and thus can be used to analyze

the design optimization for the improvement of battery performance.

4. Effect of design parameters

In the electrode design, the electrode thickness, electroactive area, porosity, and active material loading are significant parameters that affect discharge performance. For a given electrode material, the energy density of the battery can be affected by changing the electrode thickness, the electrode porosity, the active material loading. At the same time, the electrolyte concentration also has a certain influence on performance. Based on the above-established one-dimensional isothermal model of a zinc-cobalt battery, the above influencing factors are analyzed in detail.

4.1 Effect of positive electrode thickness

Although the electrode thickness is a significant design parameter that affects the discharge performance of the battery, the detailed quantitative experimental results related to the electrode thickness are relatively few. To this end, we studied the influence of thickness for the design of high-performance electrodes. As the loading of the active material can greatly affect the electrochemical performance, with the thickness changes, two scenarios are considered, including the loading keeps constant and the loading varies with the thickness proportionally.

4.1.1 Thickness and active material loading vary proportionally

When thickness and active material loading vary proportionally, the parameters associated with the change are listed in **Table 2**.

Fig. 3a exhibits the comparison of discharge curves of electrodes with different thicknesses and loadings at a current density of 5 A g^{-1}. Due to the active material loading

changes with the thickness proportionally, the electrode porosity, electroactive area, and initial concentration of CoO_2 do not change. When the electrode thickness increases from 0.1 cm to 0.2 cm, the diffusion distance becomes longer and the concentration polarization intensifies. Thus, the battery with a thicker electrode has higher internal resistance, and its output capacity is lower than that of the battery with a thinner electrode. The initial potential of discharge reaction decreases from 1.86 V to 1.82 V. With an increase of the electrode thickness, the diffusion distance of ions becomes longer, which restricts the diffusion and leads to insufficient utilization of active material. Meanwhile, with an increase of the electrode thickness, the resistance of electron transfer also increases, making it difficult to carry out the reaction away from the current collector, resulting in a capacity loss. The changes of ion diffusion and electron transport resistance with varying thickness are shown in **Fig. S3a**, which can verify the above-mentioned discussion.

4.1.2 Active material loading is constant and thickness varies

The porosity of the electrode is bound to change when the active material loading is constant but the thickness changes. When selecting electrode materials, electrode porosity is important since it can directly affect the transport of electrolyte inside the electrode, and also affect the active areas for reaction and conductivity. When the active material loading is constant and the thickness changes, the process of the parameter calculation is demonstrated in the Supporting Information, and the results are listed in **Table 3**.

Fig. 3b exhibits the comparison of discharge curves of electrodes with different thicknesses at a current density of 5 A g^{-1}. With an increase of the electrode thickness, the initial potential of discharge reaction increases from 1.82 V to 1.86 V due to the increase of

porosity and electroactive area. And, the capacity loss may come from the limitation of ion diffusion and the increase of electron transport resistance in the electrode. When the electrode thickness increases from 0.1 cm to 0.2 cm, the diffusion distance of ions becomes longer, which restricts the diffusion and leads to insufficient utilization of electrolyte ions. Meanwhile, the resistance of electron transfer also increases. Thus, the ion diffusion and electron transport resistance are important factors affecting the discharge performance of the battery.

By comparing **Figs. 3a** and **3b**, it can be found that the specific capacity of the two both increases when the electrode thickness decreases, however, the discharge voltage shows different behaviors: it decreases when the active material loading and the electrode thickness increase proportionally, but increases when the loading keeps constant as the latter case has larger electroactive area and porosity.

4.2 Effect of active material loading

For the positive electrode with a given thickness, the active material loading will change the electrode porosity and electroactive area. Herein, the impact of active material loading is investigated. The process of the parameter calculation is demonstrated in the Supporting Information, and the results are listed in **Table 4**.

Fig. 4 exhibits the comparison of discharge curves of the electrodes with different loadings at a current density of 5 A g^{-1}. When the active material loading increases, the initial discharge potential decreases from 1.93 V to 1.78 V due to the decrease of the electroactive area and porosity. In consequence, the utilization ratio of the active material decreases, which leads to a decrease of the capacity. **Fig. S3b** indicates that the larger the active material loading, the higher the electron and ion transport resistance. Thus, a low loading is preferred

to achieve a high specific capacity. It is worth noting that a high capacity is needed for practical applications, to achieve which increasing the active material loading is a general method. Therefore, an optimal loading should be selected to balance the specific and practical capacities.

4.3 Effect of separator thickness

Fig. 5 exhibits the comparison of discharge curves of different separator thicknesses at a current density of 5 A g^{-1}. As the thickness of the separator increases, the resistance of electrolyte ion transport increases. In consequence, the discharge voltage and the battery capacity decrease, but the change range is slight. This result turns out that the thickness of the separator has hardly impact on the discharge performance of the battery at some range. It is worth noting that zinc dendrite may grow during the charge process, which may reach the positive electrode and cause the internal short-circuit. To this end, the thickness can affect not only the package of the battery but also the operation safety, and thus should be well designed considering other impacts.

4.4 Effect of electrolyte concentration

In the aqueous electrolyte battery, the concentration of electrolyte influences the ionic conductivity, which further influences the rate performance of a battery. To make aqueous electrolyte-based batteries economically viable, the electrolytes with good ionic conductivity are needed to enhance ion transport for reducing the ionic polarization. Therefore, it is necessary to study the relationship among electrolyte concentration, ionic conductivity, and ionic diffusion coefficient. Gilliam et al. have established an empirical correlation for the KOH solution in the 0-12 M concentration range at 0-100 ^{o}C [38]:

$$\kappa = A(M) + B(M^2) + C(M \cdot T) + D(M / T) + E(M^3) + F(M^2 \cdot T^2) \quad (18)$$

where κ is electrolyte conductivity, *M* is the molar concentration of KOH solution (mol L^{-1}), and the values for constant A to F are -2.041, -0.0028, 0.005332, 207.2, 0.001043, and -0.0000003, respectively. Xiao et al. studied the relationship between conductivity and ionic diffusion coefficient with the following equation [39]:

$$\kappa = DcF^2 / RT \quad (19)$$

where *D* is the ionic diffusion coefficient, *c* is electrolyte concentration. Based on the above relationship, the corresponding electrolyte conductivity and ion diffusion coefficient can be obtained when the electrolyte concentration changes, as listed in **Table 5**.

Fig. 6 exhibits the comparison of discharge curves of different electrolyte concentrations at a current density of 5 A g^{-1}. The discharge potential increases due to the increase of the electrolyte concentration, and the initial potential increases from 1.83 V to 1.84 V. As the concentration increases, on the one hand, the conductivity increases; on the other hand, the viscosity increases as well, which decreases the diffusion coefficient. Under the present circumstance, the increase of conductivity seems to compensate for the decrease of the diffusion coefficient, leading to an increase of the discharge potential. However, the battery capacity is almost unchanged. Thus, using the electrolyte with a high concentration is beneficial for the improvement of the output voltage.

We also studied the effects of different design parameters on the discharge performance at another current density of 8 A g^{-1}. As the results shown in **Figs. S4-S7**, even at different current densities the conclusion is consistent.

5. Conclusions

In this work, we have made a theoretical investigation of the discharge behavior of an alkaline zinc-cobalt battery. A mathematical model has been established based on a single-domain method. The simulated discharge voltage curves with a cut-off voltage of 1.4 V agree well with the experimental results. Based on this mathematical model, the impacts of active material loading, electrode thickness, separator thickness, and electrolyte concentration on the operation performance have been investigated in detail. The specific capacity increases when the electrode thickness decreases owing to the decreased transport route for electrolyte ions. However, the discharge voltage shows different behaviors: it decreases when the loading and the electrode thickness increase proportionally, but increases when the loading keeps constant. For a given electrode thickness, both the specific capacity and the discharge voltage decrease when the active material loading increases. The separator thickness has little effect on the discharge performance of the zinc-cobalt battery. While the discharge voltage increases slightly when the electrolyte concentration increases. Hence, choosing proper electrode thickness, active material loading, and electrolyte concentration is crucial to obtain a higher discharge voltage and a larger capacity. Owing to the similar configurations and reaction mechanisms of alkaline zinc-based batteries such as Zn-AgO and Zn-Ni batteries, the present mathematical method can be transferable by adjusting the corresponding parameters, and the conclusion on the battery and electrode design can also be extended. While considering zinc-air and hybrid zinc batteries [40] which are half-open systems with the adsorption of oxygen from ambient air, new models need to be developed to offering design guidance, which is our next research topic.

Acknowledgment

P. Tan thanks the funding support from CAS Pioneer Hundred Talents Program (KJ2090130001), USTC Research Funds of the Double First-Class Initiative (YD2090002006), Joint Laboratory for USTC and Yanchang Petroleum (ES2090130110), and USTC Tang Scholar. Z. Wu thanks the funding support from Hong Kong Scholar Program (XJ2017023). M. Ni thanks the funding support from The Hong Kong Polytechnic University (G-YW2D) and a grant (Project Number: PolyU 152214/17E) from Research Grant Council, University Grants Committee, Hong Kong SAR.

Nomenclature

a	specific electroactive area ($m^2\ m^{-3}$)
A_k	boundary of phase k (m)
$\vec{B}$	body force ($N\ m^{-1}$)
c_k	molar concentration of phase k ($mol\ m^{-3}$)
c_{OH}	molar concentration of OH ($mol\ m^{-3}$)
D	diffusion coefficient ($m^2\ s^{-1}$)
D_a	dispersion coefficient ($m^2\ s^{-1}$)
E^o	overall potential of a cell (V)
F	Faraday constant (96,485 $C\ mol^{-1}$)
I	applied current density ($A\ m^{-2}$)
$\vec{i_k}$	current density vector in phase k ($A\ m^{-2}$)
i_{nj}	transfer current density of reaction j ($A\ m^{-2}$)
i_{oj}	exchange current density of reaction j ($A\ m^{-2}$)
J_{km}^{d}	interfacial species transfer rate due to diffusion ($mol\ m^{-3}\ s^{-1}$)
J_{km}^{Γ}	interfacial species transfer rate due to interface movement ($mol\ m^{-3}\ s^{-1}$)
J	transfer current density ($A\ m^{-2}$)
k	conductivity of liquid ($S\ m^{-1}$)
l	diffusion length (m)
M	molar density ($mol\ m^{-3}$)
MW	molecular weight of species ($kg\ mol^{-1}$)
N_k	molar species flux in phase k ($mol\ m^{-2}\ s^{-1}$)
N	number of transfered electron
P_k	pressure of phase k (Pa)

R	Universal gas constant (8.314 J mol^{-1} K^{-1})
r	the rate of generation of species at interface
T	temperature (K)
t	time
t_-^o	transference number of OH with respect to the solvent velocity
U_j	open-circuit overpotential for reaction j (V)
V_k	volume of phase k (m^3)
$\overrightarrow{v_k}$	velocity vector of phase k (m s^{-1})
$\overrightarrow{w_k}$	velocity of boundary of phase k (m s^{-1})
x	distance along cell sandwich width (m)
z	charge number

Greek

α_{aj}	The anodic transfer coefficient for reaction j
α_{cj}	The cathodic transfer coefficient for reaction j
ε	porosity
Γ_{km}	phase transformation rate j (V)
ρ_k	density of phase k (kg m^{-3})
σ	conductivity of solid matrix (S m^{-1})
ν	stoichiometric coefficient
τ_k	stress tensor of phase k (Pa)
ϕ	electric potential (V)

Superscripts and subscripts

avg	average
D	pertinent to diffusion
e	electrolyte phase
eff	effective, corrected for tortuosity
o	initial value, reference value
j	reaction j
ref	reference
s	solid phase
se	solid-electrolyte interface
tot	total

References

[1] B. Dunn, H. Kamath, J.M. Tarascon, B. Dunn, H. Kamath, J.-M. Tarascon, Electrical Energy Storage for the Grid: A.Battery of Choices, Science. 334 (2011) 928–935. https://doi.org/10.1126/science.1212741.

[2] P. Tan, B. Chen, H. Xu, H. Zhang, W. Cai, M. Ni, M. Liu, Z. Shao, Flexible Zn- and Li-air batteries: Recent advances, challenges, and future perspectives, Energy Environ. Sci. 10 (2017) 2056–2080. https://doi.org/10.1039/c7ee01913k.

[3] S.C. Singhal, Advances in solid oxide fuel cell technology, Solid State Ionics. 135 (2000) 305–313. https://doi.org/10.1016/S0167-2738(00)00452-5.

[4] A. Yoshino, The birth of the lithium-ion battery, Angew. Chem. Int. Ed. 51 (2012) 5798–5800. https://doi.org/10.1002/anie.201105006.

[5] R. Marom, S.F. Amalraj, N. Leifer, D. Jacob, D. Aurbach, A review of advanced and practical lithium battery materials, J. Mater. Chem. 21 (2011) 9938–9954. https://doi.org/10.1039/c0jm04225k.

[6] W. Shang, W. Yu, P. Tan, B. Chen, H. Xu, M. Ni, A high-performance Zn battery based on self-assembled nanostructured $NiCo_2O_4$ electrode, J. Power Sources. 421 (2019) 6–13. https://doi.org/10.1016/j.jpowsour.2019.02.097.

[7] G. Girishkumar, B. Mccloskey, A.C. Luntz, S. Swanson, W. Wilcke, Lithium-Air Battery: Promise and Challenges, J. Phys. Chem. 1 (2010) 2193–2203. https://doi.org/10.1021/jz1005384.

[8] C.K. Chan, H. Peng, G. Liu, K. Mcilwrath, X.F. Zhang, R.A. Huggins, Y. Cui, High-performance lithium battery anodes using silicon nanowires, Nat. Nanotechnol. 3 (2007) 31–35. https://doi.org/10.1038/nnano.2007.411.

[9] C. Wang, H. Wu, Z. Chen, M.T. Mcdowell, Y. Cui, Z. Bao, Self-healing chemistry enables the stable operation of silicon microparticle anodes for high-energy lithium-ion batteries, Nat. Chem. 5 (2013) 1042–1048. https://doi.org/10.1038/NCHEM.1802.

[10] N. Choi, Z. Chen, S.A. Freunberger, X. Ji, K. Sun, K. Amine, G. Yushin, L.F. Nazar, J. Cho, P.G. Bruce, Challenges Facing Lithium Batteries and Electrical Double-Layer Capacitors Angewandte, Angew. Chem. Int. Ed. 51 (2012) 9994–10024. https://doi.org/10.1002/anie.201201429.

[11] R. Schmuch, R. Wagner, G. Hörpel, T. Placke, M. Winter, Performance and cost of materials for lithium-based rechargeable automotive batteries, Nat. Energy. 3 (2018) 267–278. https://doi.org/10.1038/s41560-018-0107-2.

[12] E. Environ, L. Ji, M. Rao, S. Aloni, L. Wang, J. Cairns, Y. Zhang, Porous carbon nanofiber-sulfur composite electrodes for lithium/sulfur cells, Energy Environ. Sci. 4 (2011) 5053–5059. https://doi.org/10.1039/c1ee02256c.

[13] Z.P. Cano, D. Banham, S. Ye, A. Hintennach, J. Lu, M. Fowler, Z. Chen, Batteries and fuel cells for emerging electric vehicle markets, Nat. Energy. 3 (2018) 279–289. https://doi.org/10.1038/s41560-018-0108-1.

[14] Y. Li, H. Dai, Recent advances in Zinc-air batteries, Chem. Soc. Rev. 43 (2014) 5257–5275. https://doi.org/10.1039/c4cs00015c.

[15] J.F. Parker, J.S. Ko, D.R. Rolison, J.W. Long, Translating Materials-Level Performance into Device-Relevant Metrics for Zinc-Based Batteries, Joule. 2 (2018) 2519–2527. https://doi.org/10.1016/j.joule.2018.11.007.

[16] D. Selvakumaran, A. Pan, S. Liang, G. Cao, A review on recent developments and challenges of cathode materials for rechargeable aqueous Zn-ion batteries, J. Mater. Chem. A. 7 (2019) 18209–18236. https://doi.org/10.1039/c9ta05053a.

[17] J.K. Seo, J. Shin, H. Chung, P.Y. Meng, X. Wang, Y.S. Meng, Intercalation and

Conversion Reactions of Nanosized β-MnO_2 Cathode in the Secondary Zn/MnO_2 Alkaline Battery, J. Phys. Chem. 122 (2018) 11177–11185. https://doi.org/10.1021/acs.jpcc.7b11685.

[18] H. Pan, Y. Shao, P. Yan, Y. Cheng, K.S. Han, Z. Nie, C. Wang, J. Yang, X. Li, P. Bhattacharya, K.T. Mueller, J. Liu, Reversible aqueous zinc/manganese oxide energy storage from conversion reactions, Nat. Energy. 1 (2016) 1–7. https://doi.org/10.1038/NENERGY.2016.39.

[19] D. Chao, W. Zhou, C. Ye, Q. Zhang, Y. Chen, L. Gu, K. Davey, S.Z. Qiao, An Electrolytic Zn–MnO_2 Battery for High-Voltage and Scalable Energy Storage, Angew. Chem. Int. Ed. 58 (2019) 7823–7828. https://doi.org/10.1002/anie.201904174.

[20] Y. Zhong, X. Xu, J.P. Veder, Z. Shao, Self-Recovery Chemistry and Cobalt-Catalyzed Electrochemical Deposition of Cathode for Boosting Performance of Aqueous Zinc-Ion Batteries, IScience. 23 (2020) 100943. https://doi.org/10.1016/j.isci.2020.100943.

[21] P. Tan, B. Chen, H. Xu, W. Cai, M. Liu, Z. Shao, M. Ni, Nanoporous NiO/$Ni(OH)_2$ Plates Incorporated with Carbon Nanotubes as Active Materials of Rechargeable Hybrid Zinc Batteries for Improved Energy Efficiency and High-Rate Capability, J. Electrochem. Soc. 165 (2018) A2119–A2126. https://doi.org/10.1149/2.0481810jes.

[22] X. Wang, M. Li, Y. Wang, B. Chen, Y. Zhu, Y. Wu, A Zn-NiO rechargeable battery with long lifespan and high energy density, J. Mater. Chem. A. 3 (2015) 8280–8283. https://doi.org/10.1039/c5ta01947h.

[23] H. Chen, Z. Shen, Z. Pan, Z. Kou, X. Liu, H. Zhang, Q. Gu, C. Guan, J. Wang, Hierarchical Micro-Nano Sheet Arrays of Nickel–Cobalt Double Hydroxides for

High-Rate Ni–Zn Batteries, Adv. Sci. 6 (2019) 1802002. https://doi.org/10.1002/advs.201802002.

[24] P. Tan, B. Chen, H. Xu, W. Cai, W. He, H. Zhang, M. Liu, Z. Shao, M. Ni, Integration of Zn−Ag and Zn−Air Batteries: A Hybrid Battery with the Advantages of Both, ACS Appl. Mater. Interfaces. 10 (2018) 36873–36881. https://doi.org/10.1021/acsami.8b10778.

[25] D. Ozgit, P. Hiralal, G.A.J. Amaratunga, Improving Performance and Cyclability of Zinc−Silver Oxide Batteries by Using Graphene as a Two Dimensional Conductive Additive, ACS Appl. Mater. Interfaces. 6 (2014) 20751–20757. https://doi.org/10.1021/am504932j.

[26] R. Kumar, J. Shin, L. Yin, J. You, Y.S. Meng, J. Wang, All-Printed, Stretchable Zn-Ag_2O Rechargeable Battery via Hyperelastic Binder for Self-Powering Wearable Electronics, Adv. Energy Mater. 7 (2017) 1602096. https://doi.org/10.1002/aenm.201602096.

[27] Z. Wang, Z. Wu, N. Bramnik, S. Mitra, Fabrication of high-performance flexible alkaline batteries by implementing multiwalled carbon nanotubes and copolymer separator, Adv. Mater. 26 (2014) 970–976. https://doi.org/10.1002/adma.201304020.

[28] Y. Zhong, X. Xu, W. Wang, Z. Shao, Recent Advances in Metal-Organic Framework Derivatives as Oxygen Catalysts for Zinc-Air Batteries, Batter. Supercaps. 2 (2019) 272–289. https://doi.org/10.1002/batt.201800093.

[29] X. Wang, F. Wang, L. Wang, M. Li, Y. Wang, B. Chen, Y. Zhu, L. Fu, L. Zha, L. Zhang, Y. Wu, W. Huang, An Aqueous Rechargeable Zn//Co_3O_4 Battery with High

Energy Density and Good Cycling Behavior, Adv. Mater. 28 (2016) 4904–4911. https://doi.org/10.1002/adma.201505370.

[30] P. Tan, B. Chen, H. Xu, W. Cai, W. He, M. Ni, In-situ growth of Co_3O_4 nanowire-assembled clusters on nickel foam for aqueous rechargeable Zn-Co_3O_4 and Zn-air batteries, Appl. Catal. B Environ. 241 (2019) 104–112. https://doi.org/10.1016/j.apcatb.2018.09.017.

[31] L. Ma, S. Chen, H. Li, Z. Ruan, Z. Tang, Z. Liu, Z. Wang, Y. Huang, Z. Pei, J.A. Zapien, C. Zhi, Initiating a mild aqueous electrolyte Co_3O_4 /Zn battery with 2.2 V-high voltage and 5000-cycle lifespan by a Co(iii) rich-electrode, Energy Environ. Sci. 11 (2018) 2521–2530. https://doi.org/10.1039/c8ee01415a.

[32] Z. Wang, J. Huang, Z. Guo, X. Dong, Y. Liu, Y. Wang, Y. Xia, A Metal-Organic Framework Host for Highly Reversible Dendrite-free Zinc Metal Anodes, Joule. 3 (2019) 1289–1300. https://doi.org/10.1016/j.joule.2019.02.012.

[33] X. Guo, J. Zhou, C. Bai, X. Li, G. Fang, S. Liang, Zn/MnO_2 battery chemistry with dissolution-deposition mechanism, Mater. Today Energy. 16 (2020) 100396. https://doi.org/10.1016/j.mtener.2020.100396.

[34] F.Torabi and A. Aliakbar, A Single-Domain Formulation for Modeling and Simulation of Zinc-Silver Oxide Batteries, (2012) 1986–1992. https://doi.org/10.1149/2.038212jes.

[35] I.G. Casella, M. Gatta, Study of the electrochemical deposition and properties of cobalt oxide species in citrate alkaline solutions, J. Electrochem. Chem. 534 (2002) 31–38. https://doi.org/10.1016/S0022-0728(02)01100-2.

[36] U.R.A.C. No, U.L. Pasteur, B. Lefez, J. Lopitaux, M. Lenglet, Characterization of

Spinel-Type Cobalt and Nickel Oxide Thin Films by X-Ray Near Grazing Diffraction, Transmission and Reflectance Spectroscopies, and Cyclic Voltammetry, J. Electrochem. Soc. 142 (1995) 1777–1783.

[37] M. Venkatraman, J.W. Van Zee, A model for the silver-zinc battery during high rates of discharge, J. Power Sources. 166 (2007) 537–548. https://doi.org/10.1016/j.jpowsour.2006.12.064.

[38] R.J. Gilliam, J.W. Graydon, D.W. Kirk, S.J. Thorpe, A review of specific conductivities of potassium hydroxide solutions for various concentrations and temperatures, Int. J. Hydrogen Energy. 32 (2007) 359–364. https://doi.org/10.1016/j.ijhydene.2006.10.062.

[39] L. Xiao, J. Lu, P. Liu, L. Zhuang, Determination of ionic conductivity and its impact on proton diffusion model for nickel hydroxide, J. Phys. Chem. B. 110 (2006) 2057–2063. https://doi.org/10.1021/jp0548467.

[40] P. Tan, B. Chen, H. Xu, W. Cai, W. He, M. Liu, Z. Shao, M. Ni, Co_3O_4 Nanosheets as Active Material for Hybrid Zn Batteries, Small. 14 (2018) 1–9. https://doi.org/10.1002/smll.201800225.

Figure captions

Fig. 1 Schematic diagram of a zinc-cobalt battery

Fig. 2 Comparisons of the simulated discharge curves and experimental results from Ref. [29] at different current densities.

Fig. 3 Discharge curves when (a) the thickness and the active material loading vary proportionally; (b) the active material loading is constant and the thickness changes.

Fig. 4 Discharge curve when the thickness is certain and the active material loading varies.

Fig. 5 Discharge curves of different separator thicknesses.

Fig. 6 Discharge curves at different electrolyte concentrations.

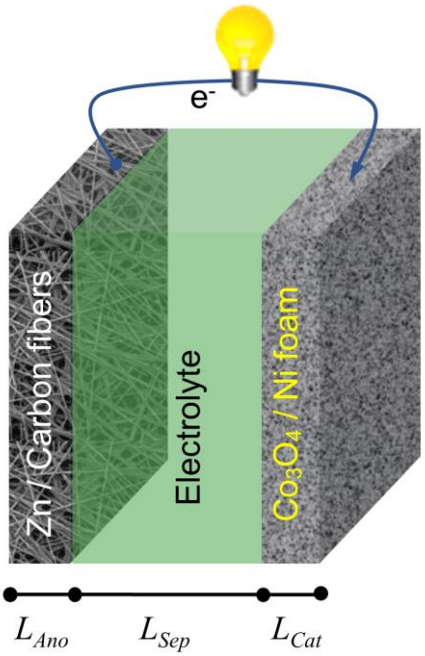

Fig. 1 Schematic diagram of a zinc-cobalt battery

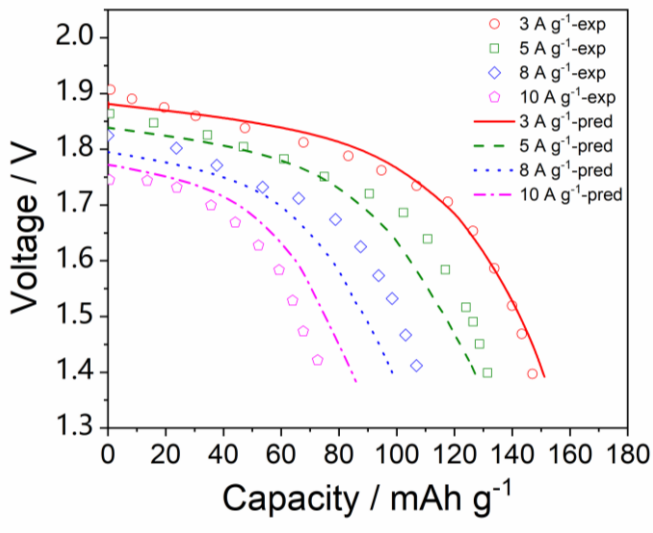

Fig. 2 Comparisons of the simulated discharge curves and experimental results from Ref. [29] at different current densities.

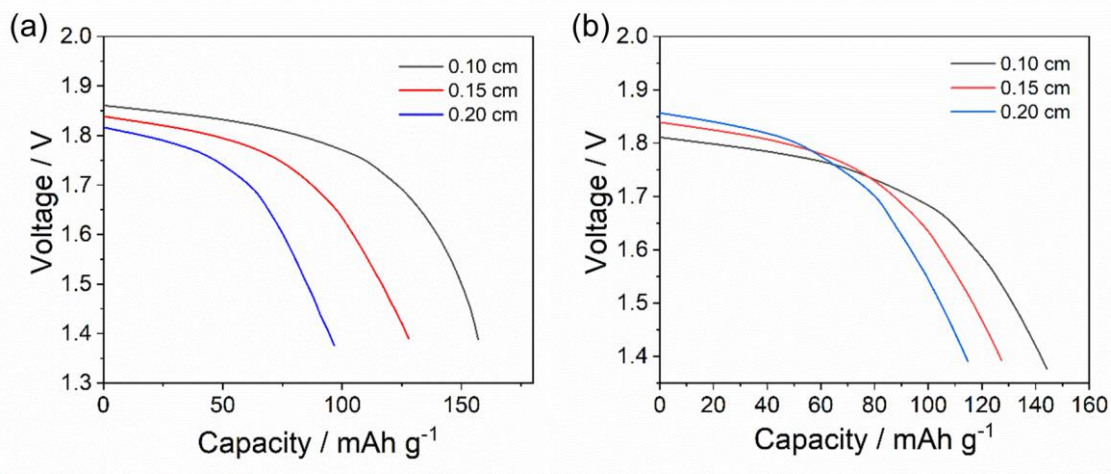

Fig. 3 Discharge curves when (a) the thickness and the active material loading vary proportionally; (b) the active material loading is constant and the thickness changes.

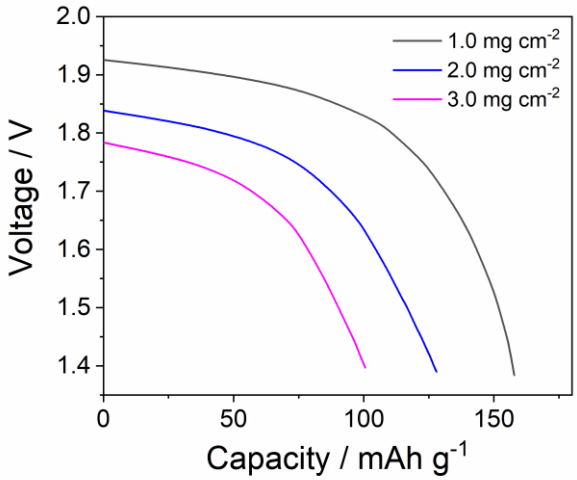

Fig. 4 Discharge curve when the thickness is certain and the active material loading varies.

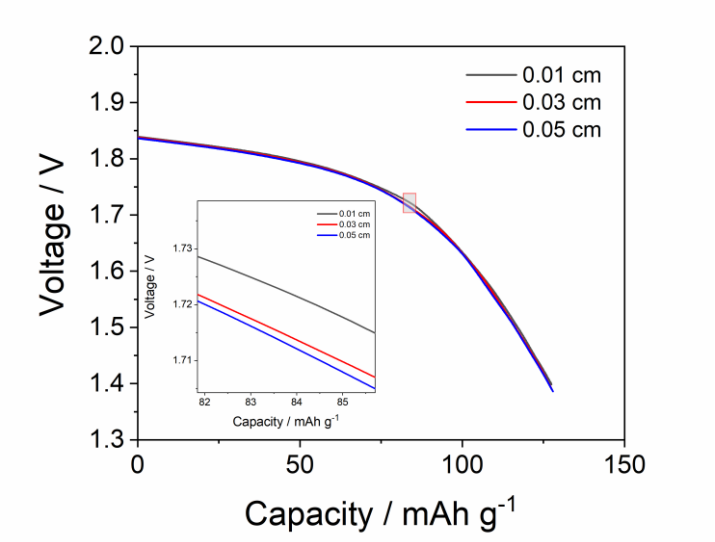

Fig. 5 Discharge curves of different separator thicknesses.

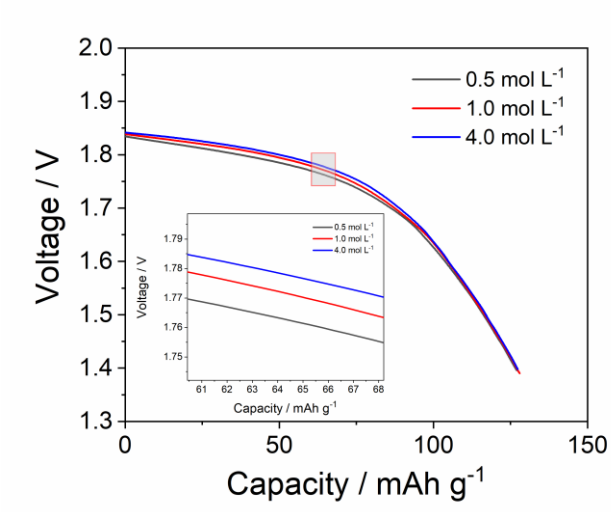

Fig. 6 Discharge curves at different electrolyte concentrations.

Table captions

Table 1 Parameters used in simulation

Table 2 The parameters for the positive electrode with the active material loading changing with the thickness

Table 3 The parameters for the positive electrode with a given active material loading

Table 4 The parameters for the positive electrode with a given thickness

Table 5 The conductivity and ion diffusion coefficients at different concentrations

Table 1 Parameters used in simulation

Parameter	Symbol	Value	Unit	Ref.
Geometrical properties				
Thickness of the separator	L_{Sep}	2×10^{-4}	m	
Thickness of the anode	L_{Ano}	3×10^{-4}	m	
Thickness of the cathode	L_{Cat}	1.5×10^{-3}	m	
Porosity of the separator	$\varepsilon_{\mathrm{Sep}}$	0.5	-	
Porosity of the anode	ε_{Ano}	0.4	-	
Porosity of the cathode	ε_{Cat}	0.8	-	
Specific surface area of the anode	a_{Ano}	1.0×10^{5}	$\mathrm{m^2\ m^{-3}}$	
Specific surface area of the cathode	a_{Cat}	2.2×10^{5}	$\mathrm{m^2\ m^{-3}}$	
Active material load	m	2	$\mathrm{mg\ cm^{-2}}$	[29]
Electrolyte properties				
Initial electrolyte concentration	$c_{l,\mathrm{int}}$	1000	$\mathrm{mol\ m^{-3}}$	[29]
Reference electrolyte concentration	$c_{\mathrm{OH,ref}}$	1000	$\mathrm{mol\ m^{-3}}$	[29]
Diffusion coefficient of OH^-	$D_{\mathrm{OH^-}}$	5.77×10^{-9}	$\mathrm{m^2\ s^{-1}}$	[39]
Diffusion coefficient of K^+	$D_{\mathrm{K^+}}$	2.15×10^{-9}	$\mathrm{m^2\ s^{-1}}$	[34]
Density of the electrolyte	ρ	1500	$\mathrm{kg\ m^{-3}}$	
Transport number	t_-^o	0.38	-	
Kinetic parameter				
Exchange current density of reaction 1	i_{01}	1×10^{-2}	$\mathrm{A\ m^{-2}}$	
Exchange current density of reaction 2	i_{02}	3×10^{-3}	$\mathrm{A\ m^{-2}}$	
Exchange current density of reaction 3	i_{03}	5×10^{-2}	$\mathrm{A\ m^{-2}}$	
The anodic charge transfer coefficients of reaction 1	α_{a1}	0.5	-s	Assumed
The cathode charge transfer coefficients of reaction 1	α_{c1}	0.5	-	Assumed
The anodic charge transfer coefficients of reaction 2	α_{a2}	0.4	-	Assumed
The cathode charge transfer coefficients of reaction 2	α_{c2}	0.6	-	Assumed
The anodic charge transfer coefficients of reaction 3	α_{a3}	0.6	-	Assumed

The cathode charge transfer coefficients of reaction 3	α_{c3}	0.4	-	Assumed
General parameter				
Density of Co_3O_4	$\rho_{Co_3O_4}$	6,050	kg m^{-3}	
Density of CoO_2	ρ_{CoO_2}	6,450	kg m^{-3}	
Density of CoOOH	ρ_{CoOOH}	2,900	kg m^{-3}	
Density of Zn	ρ_{Zn}	7,140	kg m^{-3}	
Density of ZnO	ρ_{ZnO}	5,606	kg m^{-3}	
Molar mass of Potassium ion	M_{K+}	39.1	g mol^{-1}	
Molar mass of OH ion	M_{OH-}	17.0	g mol^{-1}	
Molar mass of solvent	M_{H20}	18.0	g mol^{-1}	
Molecular weight of Co_3O_4	MW_{Co3O4}	240.79	g mol^{-1}	
Molecular weight of CoO_2	MW_{CoO2}	90.93	g mol^{-1}	
Molecular weight of CoOOH	MW_{CoOOH}	91.93	g mol^{-1}	
Molecular weight of Zn	MW_{Zn}	65.41	g mol^{-1}	
Molecular weight of ZnO	MW_{ZnO}	81.41	g mol^{-1}	
Conductivity of Co_3O_4	σ_{Co3O4}	0.15	S m^{-1}	
Conductivity of CoO_2	σ_{CoO2}	2	S m^{-1}	
Conductivity of CoOOH	σ_{CoOOH}	3	S m^{-1}	
Conductivity of Zn	σ_{Zn}	1.83×10^7	S m^{-1}	
Conductivity of ZnO	σ_{ZnO}	1	S m^{-1}	
Operating temperature	T	300	K	
Number of transferred electrons of reaction1	n_1	1	-	
Number of transferred electrons of reaction2	n_2	1	-	
Number of transferred electrons of reaction3	n_3	2	-	
Equilibrium potential of reaction1	E_{eq1}	0.37	V	[29]
Equilibrium potential of reaction1	E_{eq2}	0.464	V	[29]
Equilibrium potential of reaction1	E_{eq3}	-1.38	V	[29]
Initial concentration of zinc	$c_{Zn,init}$	5,000	mol m^{-3}	
Initial concentration of CoOOH	$c_{CoOOH,init}$	1×10^{-6}	mol m^{-3}	
Initial concentration of CoO_2	$c_{CoO_2,init}$	60	mol m^{-3}	

Table 2 The parameters for the positive electrode with the active material loading changing with the thickness

Electrode thickness (cm)	Active material loading (mg cm^{-2})	Porosity	Concentration of CoO_2 (mol m^{-3})	Electroactive area (cm^2 cm^{-3})
0.10	1.33	0.8	60	2.20×10^5
0.15	2.00	0.8	60	2.20×10^5
0.20	2.67	0.8	60	2.20×10^5

Table 3 The parameters for the positive electrode with a given active material loading

Electrode thickness (cm)	Active material loading (mg cm^{-2})	Porosity	Concentration of CoO_2 (mol m^{-3})	Electroactive area (cm^2 cm^{-3})
0.10	2	0.7989	90	1.47×10^5
0.15	2	0.8000	60	2.20×10^5
0.20	2	0.80055	45	2.93×10^5

Table 4 The parameters for the positive electrode with a given thickness

Electrode thickness (cm)	Active material loading (mg cm^{-2})	Porosity	Concentration of CoO_2 (mol m^{-3})	Electroactive area (cm^2 cm^{-3})
0.15	1	0.8011	30	4.40×10^5
0.15	2	0.8000	60	2.20×10^5
0.15	3	0.7989	90	1.47×10^5

Table 5 The conductivity and ion diffusion coefficients at different concentrations

Electrolyte concentration (mol L^{-1})	Conductivity (S cm^{-1})	Diffusion coefficient (m^2 s^{-1})
0.5	0.1146	6.14×10^{-9}
1.0	0.2153	5.77×10^{-9}
4.0	0.5700	3.82×10^{-9}